

Wavelength-selective nonlinear wavefront control in resonant thin-film lithium niobate metasurfaces

Madona Mekhail^{*1}, Timo Stolt^{*1,2}, Helena Weigand³, Kiia Arola¹, Rachel Grange³,
Patrice Genevet^{4,5}, and Mikko J. Huttunen¹

¹*Photonics Laboratory, Physics Unit, Tampere University, FI-33014 Tampere, Finland*

²*Department of Applied Physics, Aalto University, Aalto FI 00076, Espoo, Finland*

³*Optical Nanomaterial Group, Institute for Quantum Electronics, Department of Physics, ETH Zurich,
CH-8093 Zurich, Switzerland*

⁴*Université Côte d'Azur, CNRS, CRHEA, 06560 Valbonne, France*

⁵*Physics Department, Colorado School of Mines, Golden, Colorado 80401, USA*

Contact: madona.mekhail@tuni.fi

^{*}These authors contributed equally to this work

Abstract

Nonlinear metasurfaces offer compact control over frequency conversion and wavefront shaping. However, existing approaches—often based on geometric phase—lack wavelength selectivity, resulting in static nonlinear responses. Here, we demonstrate a thin-film lithium niobate metasurface that enables spectrally selective shaping of second-harmonic generation through resonance-engineered phase control. The structure consists of two regions with distinct phase responses, realized via spectral tuning of Mie-type resonances. This design enables simultaneous frequency conversion and spatial mode shaping, transforming a Gaussian pump near 1100 nm into a first-order Hermite–Gaussian mode at 550 nm, while maintaining the pump profile. The demonstrated approach offers a pathway toward ultracompact and tunable components for nonlinear holography and related applications.

Keywords: nonlinear metasurfaces, lithium niobate, wavefront shaping, second-harmonic generation, spatial mode conversion.

1 Introduction

Nonlinear optical effects are instrumental in developing light sources operating at wavelengths or time scales that are difficult to reach, and have played a key role in emergence of fields such as the generation of nonclassical light [1] and attosecond physics [2,3]. Frequency conversion processes—such as second-harmonic generation (SHG) and sum- or difference-frequency generation—are an important class of nonlinear optical effects with numerous applications, including laser amplifiers [4,5], nonlinear microscopy [6,7], quantum light source [8,9], and sensors [10–12]. Traditionally, nonlinear optical effects have been realized in macroscopic nonlinear crystals, which have strict phase-matching requirements for efficient nonlinear responses. Waveguiding media offer a more compact alternative [13–16], but their performance remains highly dependent on phase matching and is often constrained by limited tunability and narrow operation bandwidths. Moreover, they offer limited flexibility for simultaneous nonlinear conversion and wavefront shaping. To overcome these challenges, metasurfaces have emerged as a promising alternative. These ultrathin optical interfaces are composed of subwavelength structures—often called meta-atoms—that allow local control over amplitude [17,18], phase [19–21], and polarization [22,23] of light. In the nonlinear regime, metasurfaces benefit from strong local-field enhancement and relaxed phase-matching requirements, enabling highly tunable nonlinear optical processes within a very compact footprint [24].

Beyond frequency conversion, nonlinear metasurfaces offer unique capabilities for shaping the spatial profile of the interacting light. In the nonlinear regime, by engineering the phase response of individual meta-atoms, it becomes possible to tailor the wavefront of the generated nonlinear signal, enabling the generation of structured beams, such as higher order Hermite–Gaussian (HG) or Laguerre–Gaussian (LG) modes, or even full nonlinear holograms [25–29]. Metasurfaces can control the

phase of the incident light through three key mechanisms: resonant phase shifts, which depend on the phase dispersion near optical resonances [30–32], geometric (Pancharatnam–Berry) phases, which arise from the rotation of anisotropic elements under circularly polarized excitation [33,34], and propagation phases, which result from spatial variations in the optical path length due to changes in the effective refractive index across the metasurface plane [35]. While geometric phases are inherently broadband, resonant phase control offers strong wavelength selectivity and field enhancement, making it advantageous for nonlinear optical applications.

Early realizations of nonlinear metasurfaces utilized metallic nanoparticles, whose nonlinear responses are boosted by strong light confinement at the metal-dielectric interface [36–38]. Unfortunately, their performance can be limited by high ohmic losses. Dielectric metasurfaces based on III–V semiconductors with high refractive indices and intrinsic second-order nonlinearities—such as gallium arsenide [39], aluminum gallium arsenide [40], and gallium phosphide [41]—have recently emerged as low-loss alternatives, where nonlinear responses can be boosted by Mie-type resonances. . However, these materials exhibit absorption in the visible spectral range, limiting their versatility for certain nonlinear applications. In contrast, thin-film lithium niobate (TFLN) overcomes these constraints with its broad transparency window, spanning from the ultraviolet to the mid-infrared. Additionally, LN combines strong second-order nonlinearity, a high electro-optic coefficient, and low optical losses in its thin-film form, making it a widely adopted platform in integrated photonics [42–44]. Unfortunately, it can be still challenging to realize TFLN nanostructures with submicron features, due to the material’s resistance to etching. However, recent advances in nanofabrication techniques are enabling the development of TFLN-based metasurfaces, opening the door to combining its excellent bulk properties with the design flexibility of subwavelength structuring [45–49].

In this work, we combine the nonlinear optical properties of TFLN with the design flexibility of metasurfaces to demonstrate wavelength-selective spatial beam shaping of the emitted SHG signal. We design and fabricate a metasurface composed of subwavelength TFLN structures, divided in half with each half featuring different-size nanostructures. These geometry variations induce distinct resonant behaviors, resulting in a spatial phase difference between SHG signal emitted from different sides of the sample. By tailoring the phase profile of the SHG field, we realize multifunctional nonlinear metasurfaces. In particular, we demonstrate combined frequency conversion of pump beam near 1100 nm into SHG beam at 550 nm, together with mode conversion from a fundamental pump with fundamental Gaussian spatial distribution into a first-order Hermite–Gaussian SHG beam. Notably, the metasurface resonances are engineered to occur only at the SHG wavelength, ensuring that the pump beam passes through without modulation.

2 Sample design and fabrication

To identify suitable design parameters, we used Lumerical FDTD to model the optical response of TFLN nanostructures. The design process began with a parameter sweep over the lattice constant p and the nanoparticle height h , aiming to avoid diffraction at the SHG wavelength and ensuring resonance tunability. Based on both fabrication considerations and numerical results, we selected truncated nanopyrramids with different dimensions for two regions of the metasurface. In particular, dry etching of TFLN naturally leads to angled sidewalls, so this geometry ensures good agreement between the designed and fabricated structure. Representative scans from numerical simulations as well as simulations performed for the exact parameters measured in our sample are provided in the supplementary material.

The large metasurface areas of over 0.1 mm^2 were fabricated using the combination of soft nanoimprint lithography and top-down etching. This enabled to nanostructure the insulating material stack of LN on quartz without exposing the sample to electron-beam radiation and avoided the need to introduce any metallic charge dissipating layers that can introduce hard to remove impurities. In short, the desired thickness LN film was prepared, followed by the deposition of a silicon nitride hard mask film and a polymer resist soft mask film. The polymer film was molded into the designed nanostructures using thermal imprint lithography and the resulting structures were transferred to the SiN hard mask to ensure sufficient etching selectivity in comparison to the LN film. This was followed by standard LN etching process with inductive plasma etching. More fabrication details can be found in the supplementary information. The metasurfaces in this work exemplify well how the approach of utilizing imprint lithography for nanopatterning LN on inert substrates like quartz or sapphire holds

significant promise for nonlinear flat photonic devices.

As shown in Fig. 1(a), our metasurface features a lattice constant $p = 340$ nm, pyramid height $h = 135$ nm, and etch angle $\alpha_1 = 75^\circ$ for both regions. Nanoparticles in region A have side length $L_1 = 170$ nm, while region B is designed with $L_2 = 260$ nm. Based on our numerical simulations, these parameters induce a phase difference between the two regions of approximately π at a wavelength of 530 nm, which is sufficient to enable the desired mode shaping. Fig. 1(b) and (c) present the Scanning-electron microscopy (SEM) images of the fabricated TFLN metasurface, showing representative views from both regions of the sample with distinct nanoparticle geometries (L_1 and L_2). The SEM measurements revealed slight deviations from the design parameters: $L_1 \approx 252$ nm, $L_2 \approx 195$ nm, $h_1 \approx 136$ nm, and $h_2 \approx 119$ nm. The shape of the nanostructures also deviates from ideal truncated pyramids, appearing slightly distorted due to fabrication limitations such as nonuniform etching. These factors collectively impact the precision of the phase control and the fidelity of the generated spatial modes.

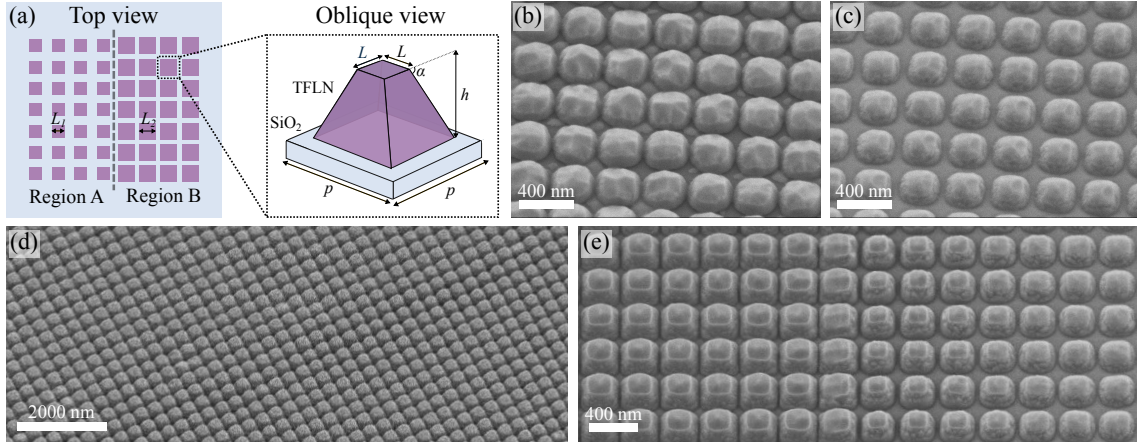


Figure 1: (a) Schematics of the metasurface, consisting of two regions (A and B) of truncated TFLN nanopyrramids with a height of $h = 135$ nm, lattice constant $p = 340$ nm and etching angle of $\alpha = 75^\circ$, and a varying side length L . The inset shows an oblique view of the unit cell. (b, c) Oblique-view SEM images of regions A ($L_1 = 195$ nm) and B ($L_2 = 252$ nm), respectively. The measured periodicity extracted from SEM data is 330 nm. (d, e) Larger-area SEM images from the interface area between regions A and B from a representative metasurface ($L_1 = 170$ nm, $L_2 = 220$ nm). SEM images were taken at a 30° tilt and prior to the removal of the silicon nitride layer on top.

3 Linear measurements and phase analysis

To characterize the metasurface, we measured the transmission spectra T of each region of the sample separately. As shown in Fig. 2(a), the extinction spectrum $\sigma_{\text{ext}} = 1 - T$ from region A reveals a Mie-type resonance near 530 nm, while region B exhibits two resonances near 530 nm and 565 nm. Due to slight deviations in dimensions and shape between the design and the fabricated nanostructures, the extracted phase response yields a shift close to π around a wavelength of 550 nm.

To extract the phase shifts associated with these resonances, we fitted a Lorentzian function to the measured extinction spectra. The extinction coefficient σ_{ext} is linked to the imaginary part of the effective polarizability α through the relation:

$$\sigma_{\text{ext}} \propto 4\pi k \text{Im}(\alpha),$$

where $k = \frac{2\pi n}{\lambda}$ is the wavenumber. Assuming that α follows a complex Lorentzian profile, we first determined $\text{Im}(\alpha)$ from the fitted transmission data. This enabled us to reconstruct the full complex polarizability α . The phase shift ϕ introduced by the resonances is then obtained from the argument of the complex polarizability:

$$\alpha = |\alpha|e^{i\varphi},$$

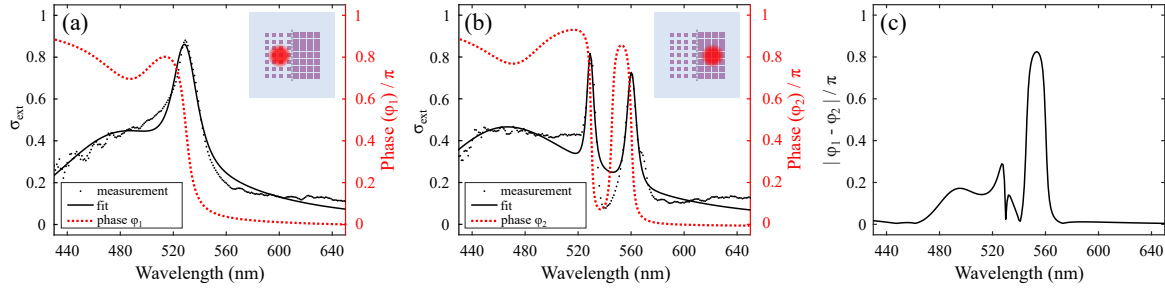


Figure 2: (a,b) Measured extinction spectra ($1 - T$) from regions A and B of the sample, corresponding to side lengths $L_1 = 170$ nm and $L_2 = 260$ nm, respectively. The plots show the experimental data (black dots), Lorentzian fits (solid dark lines), and the extracted phase responses (dotted red lines). (c) Phase difference between regions A and B in the visible spectral range.

with $\varphi = \arg(\alpha)$. These phase shifts govern the wavefront manipulation introduced by the metasurface and play a key role in shaping the transmitted light field.

As shown in Fig. 2(a) and (b), the retrieved phase shifts span a range from 0 to π . For region A, which exhibits a sharp resonance near the wavelength 530 nm, the phase response φ_1 of this resonance smoothly transitions through $\pi/2$ near the resonance wavelength. In contrast, the phase shift φ_2 in region B shows a more complex behavior due to the presence of two closely spaced resonances. The interaction between these resonances results in a rapid phase transition around 530 nm followed by a second transition near 565 nm. Note that there are no resonances at the pump wavelength range as shown from the transmission spectra at the pump wavelength range in Fig. S7 in the supplemental material.

The phase difference between the two regions $\Delta = |\varphi_1 - \varphi_2|$ governs the degree of nonlinear wavefront shaping and enables the generation of higher-order spatial modes. As shown in Fig. 2(c), at a wavelength of 550 nm, the phase difference reaches a maximum of approximately 0.85π , a condition under which we expect the interacting field to closely resemble the HG_{01} mode.

4 Nonlinear optical measurements and analysis

We experimentally verified the generation of HG_{01} mode in the SHG signal by pumping the metasurface in the wavelength range of 1000–1300 nm. The experimental setup we used is described and shown in Fig. S8 in the Supplementary material. To investigate how the SHG mode evolves across the sample, we scanned the pump beam along the x-axis from Region A to Region B in steps of approximately $20\ \mu\text{m}$, as illustrated in Fig. 3(a). When the pump is focused entirely within either region, the SHG emission exhibits a fundamental Gaussian (HG_{00}) profile. As the pump approaches the boundary between the two regions, the SHG pattern transitions into a higher-order mode consistent with the HG_{01} profile. This behavior is quantified in Fig. 3(c), which shows the overlap between the measured SHG field and an ideal HG_{01} mode, revealing a pronounced maximum near the interface. The metasurface was designed such that this mode-shaping effect is most clearly observed for a fundamental wavelength around 1100 nm.

The observed SHG pattern is shaped by the phase shifts introduced by the distinct nanoparticles geometries of the two metasurface regions. We scanned the pump wavelength and measured the SHG emission at the boundary between the two regions. As shown in Fig. 4(a), the SHG signal closely resembles the HG_{01} within the pump wavelength range of 1100–1200 nm. Fig. 4(b) shows the corresponding overlap with the ideal HG_{01} mode as a function of wavelength, highlighting a maximum near a pump wavelength of 1150 nm. This observation aligns well with theoretical predictions based on the extracted phase difference between the two metasurface regions.

It is worth noting that the measured SHG does not perfectly match the ideal HG_{01} mode. This deviation can be attributed to several factors. First, the phase difference between the SHG generated from the two regions is slightly below π , which is required for ideal mode conversion. While a full π phase shift would ideally yield a perfect HG_{01} mode, the observed deviation is likely due to the slight

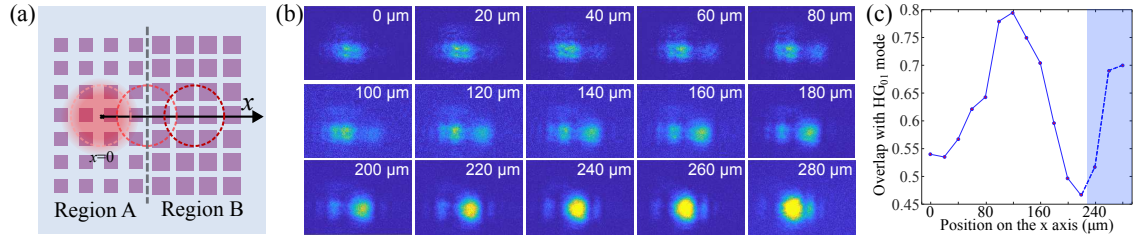


Figure 3: (a) Schematic top view of the sample, indicating the pump beam positions during the scan. The pump starts in region A and is translated along the x-axis in $20\text{ }\mu\text{m}$ steps until it reaches region B. (b) Corresponding measured SHG patterns at each pump position, showing the spatial evolution of the SHG mode from a Gaussian profile in region A, gradually transforming into an HG_{01} -like mode near the center between the two regions, and reverting back to a Gaussian profile in Region B. (c) Mode-overlap between the measured SHG field and an ideal HG_{01} mode, exhibiting a maximum near the center between the two regions. The dashed portion indicates values artificially elevated due to camera saturation.

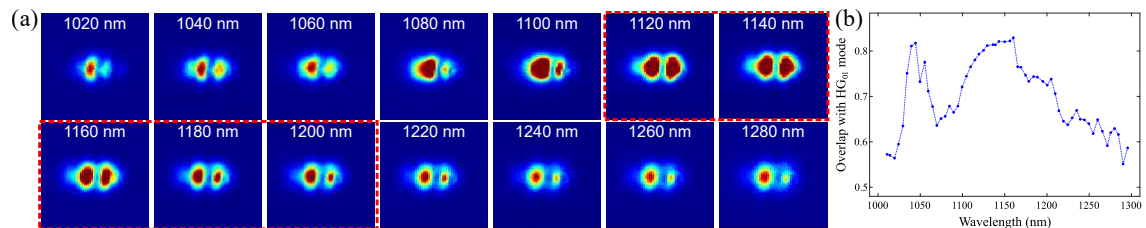


Figure 4: Left: wavelength-dependent SHG measurements. Right: the overlap with the ideal HG_{01} mode as a function of the wavelength. The best mode quality is observed for pump wavelengths between 1100—1200 nm, consistent with the expected phase difference across the metasurface.

shift of the resonances wavelengths from the design, which limits the achievable phase contrast. Second, outside the range where $\Delta\phi \approx \pi$, the SHG output is not a pure Gaussian mode but rather a diffraction pattern induced by the micrometer-scale gap between the two regions (see Fig. S5(a)). In this sense, the metasurface does not strictly convert a perfect Gaussian beam into an HG_{01} mode; rather, it modifies the diffraction pattern to approximate the desired spatial mode. Finally, the SHG intensities generated from the two regions are not perfectly balanced, leading to an asymmetric superposition and residual distortion in the output beam profile.

Our resonant-based wavefront control approach is applicable more generally than the generation of HG_{01} mode shown here. Firstly, patterning a metasurface in a more complex manner could be used for more complex structuring of generated signals. For example, a metasurface could be patterned in a radial fashion, giving rise of LG modes carrying orbital angular momentum [50]. Secondly, our approach could be used also for other processes based on wavefront control, including lensing, beam steering, and polarization state control.

In this work, we demonstrated wavefront control of SHG response at a specific wavelength. However, the broad transparency window and strong bulk nonlinearity of TFLN could be leveraged to utilize our method for numerous other nonlinear processes in a broad wavelength range. For example, difference-frequency generation and sum-frequency generation with wavelength-tunable lasers could be used with our method to realize nonlinear responses with wavelength-dependent amplitude and phase manipulation. Another approach to achieve active wavelength tunability would rely on electro-optical properties of TFLN. For example, Mie-type resonances used in this work could, in principle, be spectrally tuned by applying voltage across the metasurface. Combining this approach with collective resonances such as quasi-bound states in the continuum, surface lattice resonances, or guided-mode resonances could further enhance the electro-optic tunability and enable highly sensitive wavelength control [51–54].

[51–54]

5 Conclusions

We have experimentally demonstrated a resonance-based approach for wavelength-selective nonlinear wavefront shaping by introducing a spatially varying phase across a metasurface composed TFLN nanostructures. The metasurface features two regions with distinct meta-atom geometries, engineered to produce a distinct resonant phase behavior at the SHG wavelength range of our measurements. By analyzing the linear transmission spectra and extracting the phase response from each region, we identified a spectral window where the difference between phase shifts induced by each region approaches π —a condition that supports the formation of an HG_{01} -like mode in the SHG field. Our nonlinear measurements confirmed the formation of the higher-order HG mode at the desired wavelength of 550 nm. Beyond generation structured nonlinear responses, our approach is applicable for other processes involving wavefront shaping, such as lensing, beam steering, and holography. Future studies could also utilize strong electro-optical properties of TFLN to realize electrically tunable operation. Overall, the approach demonstrated here could pave the path to realize efficient, tunable, and multifunctional nonlinear optical components for integrated and nanophotonics.

Acknowledgments

The authors acknowledge Robert Fickler, Andriy Shevchenko, and Radoslaw Kolkowski for insightful discussions and support. T.S. acknowledges financial support from the Jenny and Antti Wihuri Foundation through a doctoral research grant and from the Emil Aaltonen Foundation through a research travel grant. The authors thank the Scientific Center for Optical and Electron Microscopy (ScopeM), the Binning and Rohrer Nanotechnology Center (BRNC), and the FIRST cleanrooms of Eidgenössische Technische Hochschule (ETH) Zurich. This work was supported by the Swiss National Science Foundation SNSF (Consolidator Grant 213713).

Author contributions

M.M. performed numerical simulations, assisted with optical measurements, analyzed the data and wrote the first version of the manuscript. T.S. designed the sample, performed optical measurements, and contributed to manuscript writing. H.W. fabricated the samples and performed SEM measurements. K.A. assisted with transmission measurements, R. G. supervised the sample fabrication. P.G., R.G. and M.H. supervised the project and contributed to manuscript revision. All authors discussed the results and contributed to the final version of the manuscript.

References

- [1] David C. Burnham and Donald L. Weinberg. Observation of simultaneity in parametric production of optical photon pairs. *Phys. Rev. Lett.*, 25(2), 1970.
- [2] P. B. Corkum. Plasma perspective on strong field multiphoton ionization. *Phys. Rev. Lett.*, 71(13), 1993.
- [3] Ferenc Krausz and Misha Ivanov. Attosecond physics. *Rev. Mod. Phys.*, 81(1), 2009.
- [4] Xuelei Fu, Xiaojie Guo, and Chester Shu. Raman-enhanced phase-sensitive fibre optical parametric amplifier. *Sci. Rep.*, 6(20180), 2016.
- [5] Pavel Sidorenko, Walter Fu, , and Frank Wise. Nonlinear ultrafast fiber amplifiers beyond the gain-narrowing limit. *Optica*, 6(10):1328–1333, 2019.
- [6] Gitanjal Deka, Chi-Kuang Sun, Katsumasa Fujita, and Shi-Wei Chu. Nonlinear plasmonic imaging techniques and their biological applications. *Nanophotonics*, 6(1):31–49, 2016.
- [7] Kobi Frischwasser, Kobi Cohen, Jakob Kher-Alden, Shimon Dolev, Shai Tsesses, and Guy Bartal. Real-time sub-wavelength imaging of surface waves with nonlinear near-field optical microscopy. *Nat. photon.*, 15:442–448, 2021.

- [8] Prem Kumar. Quantum frequency conversion. *Opt. Lett.*, 15(24):1476–1478, 1990.
- [9] Jie Zhao, Chaoxuan Ma, Michael Rüsing, and Shayan Mookherjea. High quality entangled photon pair generation in periodically poled thin-film lithium niobate waveguides. *Phys. Rev. Lett.*, 124(163603), 2020.
- [10] Martin Mesch, Bernd Metzger, Mario Hentschel, and Harald Giessen. Nonlinear plasmonic sensing. *Nano Lett.*, 16(5):3155–3159, 2016.
- [11] Mrigank Singh Verma and Manabendra Chandra. Nonlinear plasmonic sensing for label-free and selective detection of mercury at picomolar level. *ACS Sens.*, 5(3):645–649, 2020.
- [12] Renwen Yu1, Joel D. Cox1, and F. Javier García de Abajo. Nonlinear plasmonic sensing with nanographene. *Phys. Rev. Lett.*, 117:123904, 2016.
- [13] Nanfang Yu and Federico Capasso. Flat optics with designer metasurfaces. *Nat. Mater.*, 13:139–150, 2014.
- [14] Stanislav B. Glybovski, Sergei A. Tretyakov, Pavel A. Belov, Yuri S. Kivshar, and Constantin R. Simovski. Metasurfaces: From microwaves to visible. *Phys. Rep.*, 634:1–72, 2016. Metasurfaces: From microwaves to visible.
- [15] Lei Zhang, Shengtao Mei, Kun Huang, and Cheng-Wei Qiu. Advances in full control of electromagnetic waves with metasurfaces. *Adv. Opt. Mater.*, 4(6):818–833, 2016.
- [16] Weiwei Wan, Jie Gao, and Xiaodong Yang. Metasurface holograms for holographic imaging. *Adv. Opt. Mater.*, 5(21):1700541, 2017.
- [17] Isabelle Staude, Andrey E. Miroshnichenko, Manuel Decker, Nche T. Fofang, Sheng Liu, Edward Gonzales, Jason Dominguez, Ting Shan Luk, Dragomir N. Neshev, Igal Brener, and Yuri Kivshar. Tailoring directional scattering through magnetic and electric resonances in subwavelength silicon nanodisks. *ACS Nano*, 7(9):7824–7832, 2013.
- [18] P. Spinelli, M.A. Verschuuren, and A. Polman. Broadband omnidirectional antireflection coating based on subwavelength surface mie resonators. *Nat. Commun.*, 3(692), 2012.
- [19] Adam C. Overvig, Sajan Shrestha, Stephanie C. Malek, Ming Lu, Aaron Stein, Changxi Zheng, and Nanfang Yu. Dielectric metasurfaces for complete and independent control of the optical amplitude and phase. *Light Sci. Appl.*, 8(92), 2019.
- [20] Jing Li, Tiesheng Wu, Wenbin Xu, Yumin Liu, Chang Liu, Yu Wang, Zhongyuan Yu, Danfeng Zhu, Li Yu, and Han Ye. Mechanisms of 2π phase control in dielectric metasurface and transmission enhancement effect. *Opt. Express*, 27(16):23186–23196, 2019.
- [21] Song Gao, Wenjing Yue, Chul-Soon Park, Sang-Shin Lee, Eun-Soo Kim, and Duk-Yong Choi. Aluminum plasmonic metasurface enabling a wavelength-insensitive phase gradient for linearly polarized visible light. *ACS Photonics*, 4(2):322–328, 2017.
- [22] Tong Li, Xiaobin Hu, Huamin Chen, Chen Zhao, Yun Xu, Xin Wei, and Guofeng Song. Metallic metasurfaces for high efficient polarization conversion control in transmission mode. *Opt. Express*, 25(20):23597–23604, 2017.
- [23] Shuai Wang, Zi-Lan Deng, Yujie Wang, Qingbin Zhou, Xiaolei Wang, Yaoyu Cao, Bai-Ou Guan, Shumin Xiao, and Xiangping Li. Arbitrary polarization conversion dichroism metasurfaces for all-in-one full poincaré sphere polarizers. *Light Sci. Appl.*, 10(24), 2021.
- [24] Guixin Li, Shuang Zhang, and Thomas Zentgraf. Nonlinear photonic metasurfaces. *Nat. Rev. Mater.*, 2(17010), 2017.
- [25] Haoran Ren, Gauthier Briere, Xinyuan Fang, Peinan Ni, Rajath Sawant, Sébastien Héron, Sébastien Chenot, Stéphane Vézian, Benjamin Damilano, Virginie Brändli, Stefan A. Maier, and Patrice Genevet. Metasurface orbital angular momentum holography. *Nat. commun.*, 10(2986), 2019.

- [26] Shay Keren-Zur, Lior Michaeli, Haim Suchowski, and Tal Ellenbogen. Shaping light with nonlinear metasurfaces. *Adv. Opt. Photon.*, 10(1):309–353, 2018.
- [27] Euclides Almeida, Ora Bitton, and Yehiam Prior. Nonlinear metamaterials for holography. *Nat. commun.*, 7(12533):309–353, 2016.
- [28] Yisheng Gao, Yubin Fan, Yujie Wang, Wenhong Yang, Qinghai Song, and Shumin Xiao. Nonlinear holographic all-dielectric metasurfaces. *Nano Lett.*, 18(12):8054–8061, 2018.
- [29] Shay Keren-Zur, Ori Avayu, Lior Michaeli, and Tal Ellenbogen. Nonlinear beam shaping with plasmonic metasurfaces. *ACS Photonics*, 3(1):117–123, 2016.
- [30] Rémi Colom, Elena Mikheeva, Karim Achouri, Jesus Zuniga-Perez, Nicolas Bonod, Olivier J. F. Martin, Sven Burger, and Patrice Genevet. Crossing of the branch cut: The topological origin of a universal 2π -phase retardation in non-hermitian metasurfaces. *Laser & Photonics Reviews*, 17(6):2200976, 2023.
- [31] Felix Binkowski, Fridtjof Betz, Rémi Colom, Patrice Genevet, and Sven Burger. Poles and zeros in non-hermitian systems: Application to photonics. *Phys. Rev. B*, 109:045414, Jan 2024.
- [32] Elena Mikheeva, Rémi Colom, Karim Achouri, Adam Overvig, Felix Binkowski, Jean-Yves Duboz, Sébastien Cueff, Shanhui Fan, Sven Burger, Andrea Alu, and Patrice Genevet. Asymmetric phase modulation of light with parity-symmetry broken metasurfaces. *Optica*, 10:1287–1294, Oct 2023.
- [33] Ke Chen, Yijun Feng, Zhongjie Yang, Li Cui, Junming Zhao, Bo Zhu, and Tian Jiang. Geometric phase coded metasurface: from polarization dependent directive electromagnetic wave scattering to diffusion-like scattering. *Sci. Rep.*, 6(35968), 2016.
- [34] Bingyi Liu, René Geromel, Zhaoxian Su, Kai Guo, Yongtian Wang, Zhongyi Guo, Lingling Huang, and Thomas Zentgraf. Nonlinear dielectric geometric-phase metasurface with simultaneous structure and lattice symmetry design. *ACS Photonics*, 10(12):4357–4366, 2023.
- [35] Wei Ting Chen, Alexander Y. Zhu, Jared Sisler, Zameer Bharwani, and Federico Capasso. A broadband achromatic polarization-insensitive metalens consisting of anisotropic nanostructures. *Nat. Commun.*, 10(355), 2019.
- [36] David C. Hooper, Christian Kuppe, Danqing Wang, Weijia Wang, Jun Guan, Teri W. Odom, and Ventsislav K. Valev. Second harmonic spectroscopy of surface lattice resonances. *Nano Letters*, 19(1):165–172, 2019.
- [37] Tsafrir Abir, Mai Tal, and Tal Ellenbogen. Second-harmonic enhancement from a nonlinear plasmonic metasurface coupled to an optical waveguide. *Nano Lett.*, 22(7):2712–2717, 2022.
- [38] Giovanna Palermo, Massimo Rippa, Ylli Conti, Ambra Vestri, Riccardo Castagna, Giovanna Fusco, Elisabetta Suffredini, Jun Zhou, Joseph Zyss, Antonio De Luca, and Lucia Petti. Plasmonic metasurfaces based on pyramidal nanoholes for high-efficiency sers biosensing. *ACS Appl. Mater. Interfaces*, 13(36):43715–43725, 2021.
- [39] Jürgen D. Sautter, Lei Xu, Andrey E. Miroshnichenko, Mykhaylo Lysevych, Irina Volkovskaya, Daria A. Smirnova, Rocio Camacho-Morales, Khosro Zangeneh Kamali, Fouad Karouta, Kaushal Vora, Hoe H. Tan, Martti Kauranen, Isabelle Staude, Chennupati Jagadish, Dragomir N. Neshev, , and Mohsen Rahmani. Tailoring second-harmonic emission from (111)-gaas nanoantennas. *Nano lett.*, 19:3905–3911, 2019.
- [40] Giuseppe Marino, Carlo Gigli, Davide Rocco, Aristide Lemaître, Ivan Favero, Costantino De Angelis, , and Giuseppe Leo. Zero-order second harmonic generation from algaas-on-insulator metasurfaces. *ACS photonics*, 6:1226–1231, 2019.
- [41] Blaine McLaughlin, David P. Lake, Matthew Mitchell, and Paul E. Barclay. Nonlinear optics in gallium phosphide cavities: simultaneous second and third harmonic generation. *J. Opt. Soc. Am. B*, 39(7):1853–1860, 2022.

[42] R. S. Weis and T. K. Gaylord. Lithium niobate: Summary of physical properties and crystal structure. *Applied Physics A*, 37:191–203, 1985.

[43] Di Zhu, Linbo Shao, Mengjie Yu, Rebecca Cheng, Boris Desiatov, C. J. Xin, Yaowen Hu, Jeffrey Holzgrafe, Soumya Ghosh, Amirhassan Shams-Ansari, Eric Puma, Neil Sinclair, Christian Reimer, Mian Zhang, and Marko Lončar. Integrated photonics on thin-film lithium niobate. *Adv. Opt. Photon.*, 13(2):242–352, 2021.

[44] Zihan Li, Rui Ning Wang, Grigory Lihachev, Junyin Zhang, Zelin Tan, Mikhail Churaev, Nikolai Kuznetsov, Anat Siddharth, Mohammad J. Bereyhi, Johann Riemensberger, and Tobias J. Kippenberg. High density lithium niobate photonic integrated circuits. *Nat. Commun.*, 14(4856), 2023.

[45] Anna Fedotova, Luca Carletti, Attilio Zilli, Frank Setzpfandt, Isabelle Staude, Andrea Toma, Marco Finazzi, Costantino De Angelis, Thomas Pertsch, Dragomir N. Neshev, and Michele Cebrano. Lithium niobate meta-optics. *ACS Photonics*, 9(12), 2022.

[46] Runxue Leng, Xingqiao Chen, Ping Liu, Zhihong Zhu, and Jianfa Zhang. High q lithium niobate metasurfaces with transparent electrodes for efficient amplitude and phase modulation. *Appl. Opt.*, 63(12):3156–3161, 2024.

[47] Helena Weigand, Viola V. Vogler-Neuling, Marc Reig Escalé, David Pohl, Felix U. Richter, Artemios Karvounis, Flavia Timpu, and Rachel Grange. Enhanced electro-optic modulation in resonant metasurfaces of lithium niobate. *ACS Photonics*, 8(10):3004–3009, 2021.

[48] David Barton, Mark Lawrence, and Jennifer Dionne. Wavefront shaping and modulation with resonant electro-optic phase gradient metasurfaces. *Appl. Phys. Lett.*, 118(7):071104, 2021.

[49] Anna Fedotova, Mohammadreza Younesi, Jürgen Sautter, Aleksandr Vaskin, Franz J.F Löchner, Michael Steinert, Reinhard Geiss, Thomas Pertsch, Isabelle Staude, and Frank Setzpfandt. Second-harmonic generation in resonant nonlinear metasurfaces based on lithium niobate. *Nano Lett.*, 20(12):8608–8614, 2020.

[50] Alexander Faßbender, Jiří Babocký, Petr Dvořák, Vlastimil Krápek, and Stefan Linden. Invited article: Direct phase mapping of broadband laguerre-gaussian metasurfaces. *APL Photonics*, 3(11):110803, 10 2018.

[51] Aravind P Anthur, Haizhong Zhang, Ramon Paniagua-Dominguez, Dmitry A Kalashnikov, Son Tung Ha, Tobias WW Maß, Arseniy I Kuznetsov, and Leonid Krivitsky. Continuous wave second harmonic generation enabled by quasi-bound-states in the continuum on gallium phosphide metasurfaces. *Nano Letters*, 20(12):8745–8751, 2020.

[52] M. Saad Bin-Alam, Orad Reshef, Yaryna Mamchur, M. Zahirul Alam, Graham Carlow, Jeremy Upham, Brian T. Sullivan, Jean-Michel Ménard, Mikko J. Huttunen, Robert W. Boyd, and Ksenia Dolgaleva. Ultra-high- q resonances in plasmonic metasurfaces. *Nat. commun.*, 12(974), 2021.

[53] Yao Ju, Wei Zhang, and Haoyi Zuo. Promoting second-harmonic generation in the linbo3 film combined with metasurface using plasmonic quasi bound states in the continuum. *Photonics and Nanostructures - Fundamentals and Applications*, 57:101194, 2023.

[54] Subhajit Bej, Nikolai Tkachenko, Robert Fickler, and Tapani Niemi. Ultrafast modulation of guided-mode resonance in a nonlinear silicon nitride grating. *Advanced Optical Materials*, 13(7):2402632, 2025.

Supplementary material: Wavelength-selective nonlinear wavefront control in resonant lithium niobate metasurfaces

Madona Mekhael^{*1}, Timo Stolt^{*1,2}, Helena Weigand³, Kiia Arola¹, Rachel Grange³,
Patrice Genevet^{4,5}, and Mikko J. Huttunen¹

¹ *Photonics Laboratory, Physics Unit, Tampere University, FI-33014 Tampere, Finland*

² *Department of Applied Physics, Aalto University, Aalto FI 00076, Espoo, Finland*

³ *Optical Nanomaterial Group, Institute for Quantum Electronics, Department of Physics, ETH Zurich, CH-8093 Zurich, Switzerland*

⁴ *Université Côte d'Azur, CNRS, CRHEA, 06560 Valbonne, France*

⁵ *Physics Department, Colorado School of Mines, Golden, Colorado 80401, USA*

Contact: madona.mekhael@tuni.fi

^{*}These authors contributed equally to this work

1 Numerical simulations

Figures S1 and S2 show representative numerical scans of the transmission spectra and the corresponding phase responses for a fixed lattice constant $p = 340$ nm and a varying particle height between 110–170 nm. For each case, the side length L was swept and the spectral dependence of transmission and phase was extracted. These scans illustrate how the nanoparticle height and lateral dimensions influence the resonance position and the associated phase dispersion, providing the basis for selecting the final design parameters. As observed in Fig. S1, increasing the side length of the nanoparticles leads to a redshift of the resonance. At longer L values, a second resonance emerges, which can be tuned by varying the particle height. This resonance is attributed to a magnetic dipole mode oriented along the z-axis.

Figure S3 illustrates the numerical simulations of the transmission spectra and the associated phase response of light interacting with the sample parameters measured in our experiments. Following the design-process scans presented earlier, this figure highlights the specific geometrical parameters used in the fabricated sample. In Fig. S3(a), a single resonance appears near 523 nm for light interacting with region A of the sample, which has a side length of $L_1 = 170$ nm. In contrast, Fig. S3(b) shows two resonances in region B (with $L_2 = 260$ nm), located near 523 nm and 532 nm. The resulting phase difference, shown in Fig. S3(c), exhibits a peak of approximately 0.7π around 530 nm.

2 Sample fabrication and characterization

Fabrication of thin-film lithium niobate (TFLN) nanoparticles on a quartz substrate was carried out using a combination of soft-nanoimprint lithography and reactive ion-etching (RIE). A multilayer stack consisting of quartz, TFLN, silicon nitride (SiN), and a polymethyl methacrylate (PMMA) was prepared. The soft-imprint technique was employed, because of challenges to imprint large and isolated areas using direct electron-beam lithography.

As illustrated in Fig. S4, the fabrication process began with the preparation of a polydimethylsiloxane (PDMS) mold replicated from a silicon master mold patterned by electron-beam lithography. This mold was then used to transfer the nanoscale patterns onto the top PMMA layer. The transferred pattern was subsequently used as a mask for etching the SiN layer using reactive-ion etching with CHF_3 . PMMA alone was unsuitable for pattern transfer due to its low resistance to the intense ion bombardment required for etching the TFLN layer, which would lead to rapid degradation and loss of nanostructure features. Instead, PMMA was used to pattern the SiN layer, which then served as a robust hard mask for etching the TFLN nanoparticles using inductively-coupled plasma reactive-ion etching (ICP-RIE). Finally, after removing the SiN layer, this process resulted in a well-defined TFLN nanoparticles on the quartz substrate.

Fig. S5(a) presents a Scanning-electron microscopy (SEM) image showing the two regions of the sample separated by a narrow gap of approximately 4 μm , which was introduced during fabrication. This gap, a

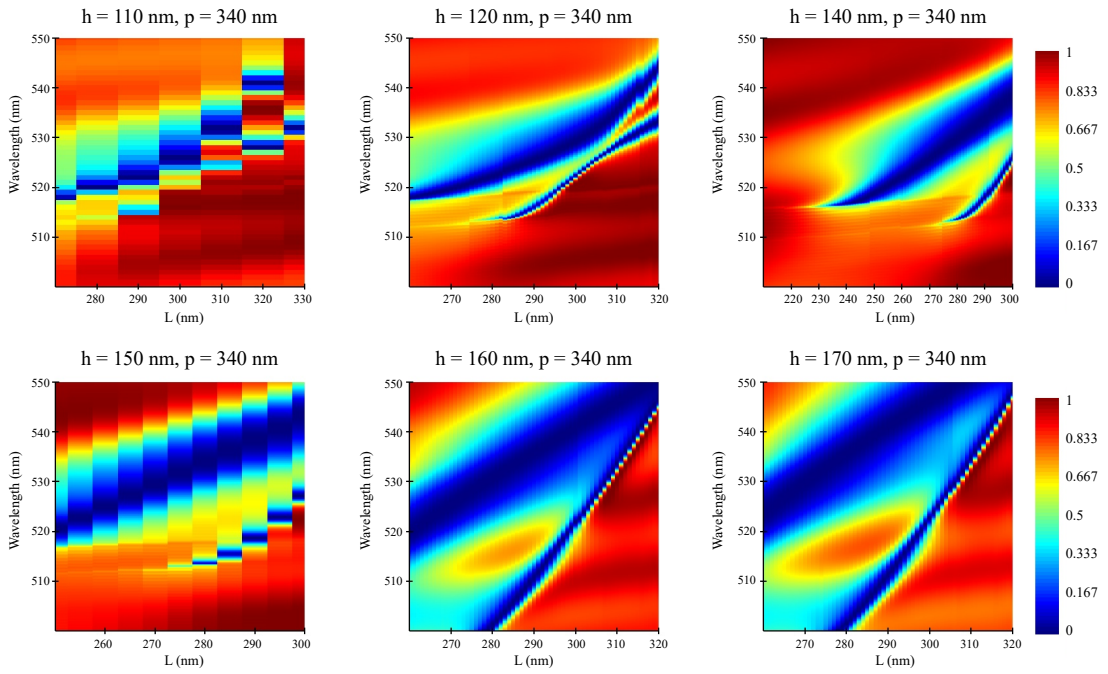


Figure S1: Transmission spectra as a function of the side length L for nanopyramid arrays with $p = 340$ nm and a varying height h .

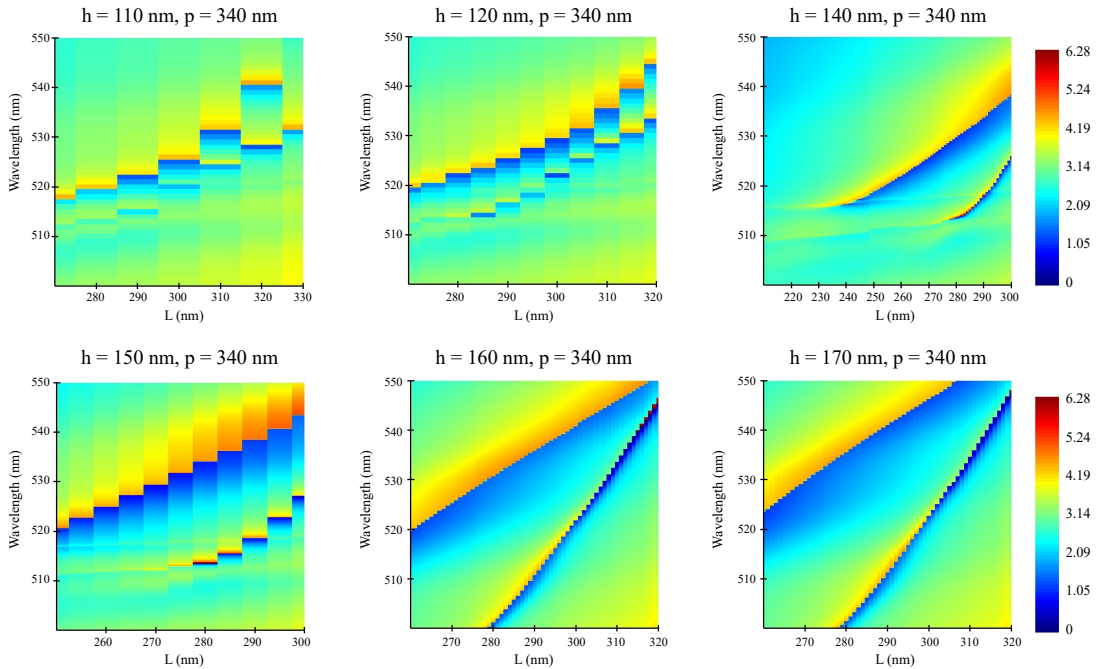


Figure S2: Corresponding phase responses as a function of the side length L for the same structures as in Fig. S1.

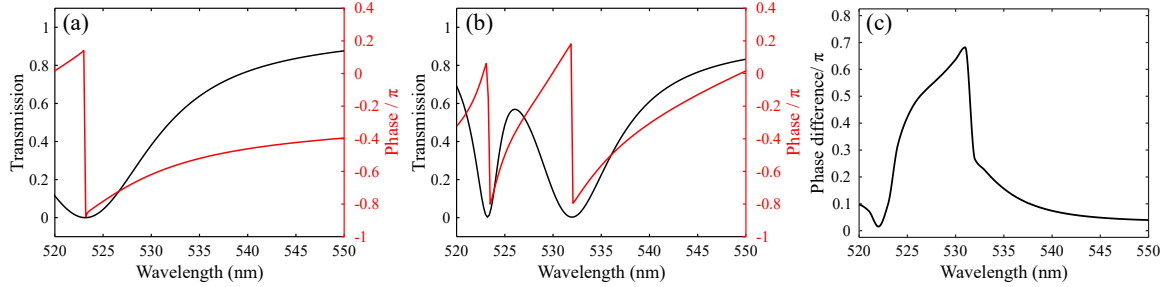


Figure S3: (a,b) Numerical simulations of the transmission spectra and the assicated phase changes from regions A and B of the sample, corresponding to side lengths $L_1 = 170$ nm and $L_2 = 260$ nm, respectively. (c) hase difference between regions A and B in the visible spectral range.)

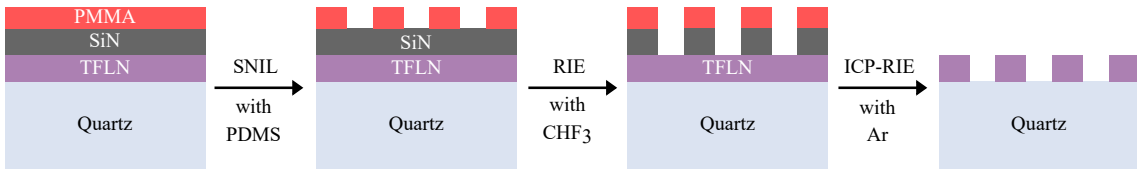


Figure S4: Fabrication steps of the TFLN nanoparticles on quartz substrate.

result of the imprint process where the resist did not fully fill the mold at geometry transitions, acts as a diffraction wire. It explains why the SHG beam profile deviates from a Gaussian shape at wavelengths far from the π —particularly when the phase difference between the two regions approaches zero. It is worth noting that the gap is less apparent in some designs with different side lengths values. Fig. S5(b) shows a large-area view of the metasurface, covering a total area of 0.15 mm^2 . To our knowledge, such a large continuous region of patterned TFLN metasurface was not previously reported.

3 Experimental setup

To measure the transmission spectra from the sample, we used the setup illustrated in Fig. S6. A white-light source covering the range 300–2600 nm provided illumination, and a broadband linear polarizer (LP) was used to control the polarization. The sample was positioned in the Fourier plane of a $4f$ system consisting of lenses L1–L4 with focal lengths $f_1 = 40$ mm, $f_2 = 18$ mm, $f_3 = 19.5$ mm, and $f_4 = 75$ mm. A flip mirror (FM) directed the beam to a camera for sample imaging, while lens L5 coupled the transmitted light into a spectrometer via a fiber coupler (FC). The transmission spectra were recorded with an AvaSpec-ULS-RS-TEC spectrometer (Avantes). Figure. S7 shows the transmission spectra from Regions A and B of the sample, indicating that no resonances are present within the pump wavelength range. Consequently, the pump beam remains unshaped, and the observed variations in the

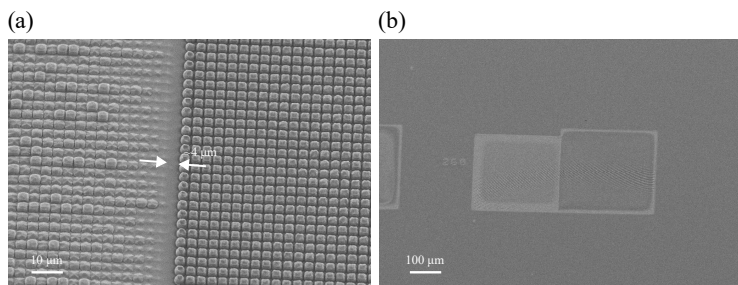


Figure S5: (a) SEM image showing the two regions of the measured sample with a fabrication-induced gap of approximately $4 \mu\text{m}$ between them, which acts as a diffraction wire distorting the spatial mode of the SHG beam. (b) Large-area SEM image of the metasurface with a total area of 0.15 mm^2 . SEM images were taken at a 30° tilt and prior to the removal of the silicon nitride layer on top.

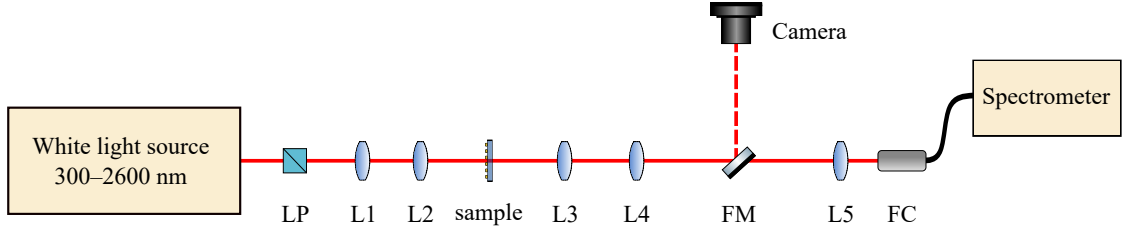


Figure S6: A schematic for the setup used to measure the transmission spectra from the sample.

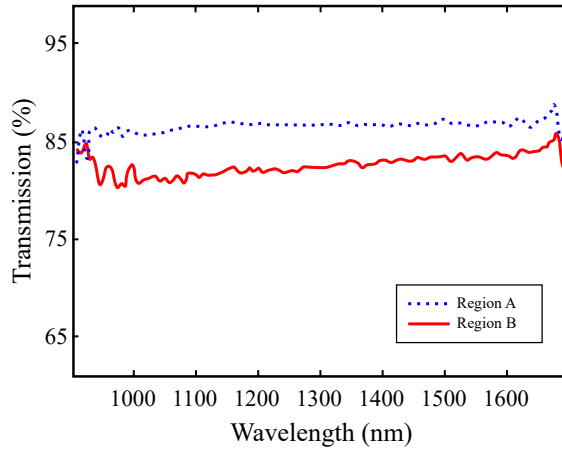


Figure S7: Transmission spectra from the two regions of the sample at the pump wavelength range.

SHG mode arise from resonances occurring at the SHG wavelength.

Figure S8 shows the experimental setup used to measure the nonlinear signal from the sample. An optical parametric oscillator (OPO) pumped by a femtosecond laser (Chameleon Vision II) served as the tunable light source, providing pulses of 220 fs duration within the 1000–1300 nm wavelength range at a repetition rate of 82 MHz. The power was controlled and stabilized during wavelength scanning using a motorized half-wave plate (HWP1) in combination with a polarizer. To ensure high beam quality, the laser beam was spatially filtered using a pair of lenses with a pinhole positioned between them, which effectively removed higher-order spatial modes before the beam interacted with the sample.

A positive lens L3 ($f = 500$ mm) lens was used to focus the pump beam onto the sample, with an additional half-wave plate (HWP2) to control its polarization. To block any unwanted light at pump wavelength range, a long-pass filter was placed before the sample. After interacting with the sample, the emitted SHG signal was separated from the fundamental beam using a dichroic mirror, which reflected the pump beam while transmitting the SHG. The reflected pump was directed through a 4f imaging system composed of lenses L4 and L5 to image the sample. Meanwhile, the transmitted SHG signal was directed toward the SHG camera for spatial mode characterization. Two consecutive 4f imaging systems, with a pinhole placed at the intermediate focal plane, were used to filter and image the SHG mode immediately after the sample. A short-pass filter was used in front of the camera to block any remaining pump light and ensure that only the SHG signal was imaged. A flip mirror (FM) was used to switch between the photomultiplier tube (PMT) to measure the strength of the signal and the SHG camera to image the spatial profile of the SHG beam. Fig. S9 shows the SHG signal measured using the PMT at the left (region A), right (region B), and the center of the sample between the two regions. The results show good agreement with the design as well as the measured transmission spectra.

To demonstrate that our device selectively shapes only the SHG signal without affecting the pump beam, we imaged the spatial profile of the pump after transmission through different parts of the sample using a beam profiler (Pyrocam III HR from Spiricon)(Fig. S10). The measurements were performed after the beam interacted either with Region A, Region B, the center between regions A and B, or a bare glass substrate. In all cases, the transmitted pump retained its Gaussian profile, confirming that the metasurface does not modify the spatial shape of the fundamental beam. This result validated that the mode shaping occurs exclusively at the SHG wavelength, as intended, and not due to any reshaping

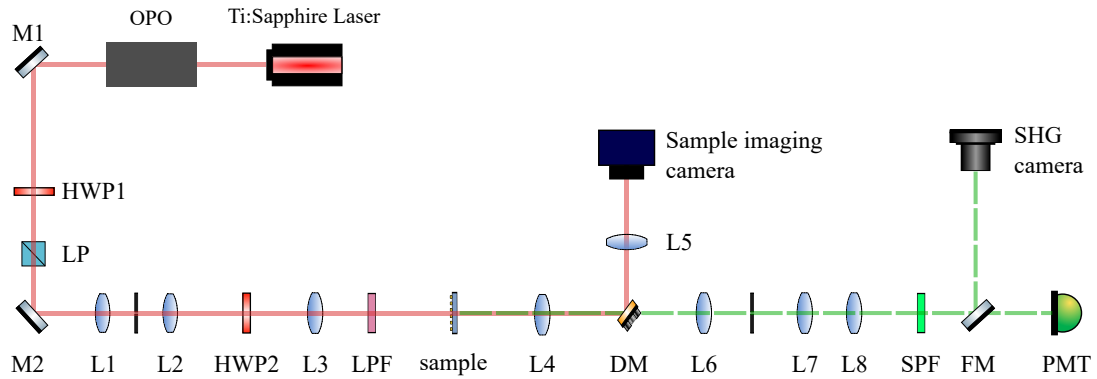


Figure S8: A schematic for the optical setup used to measure the SHG from the sample and image its spatial modes.

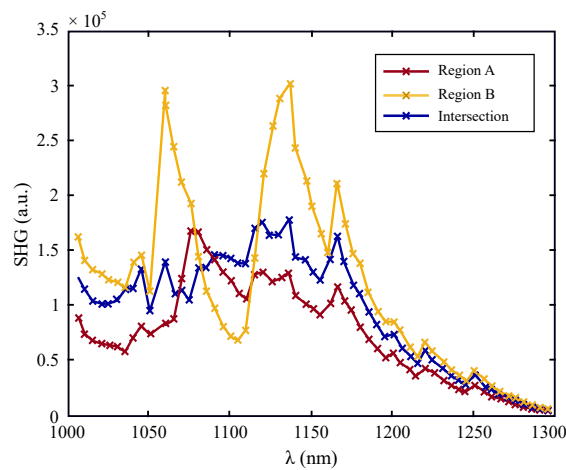


Figure S9: Measured SHG spectra from different regions of the sample. Measurements show agreement with the measured transmission spectra.

of the input beam.

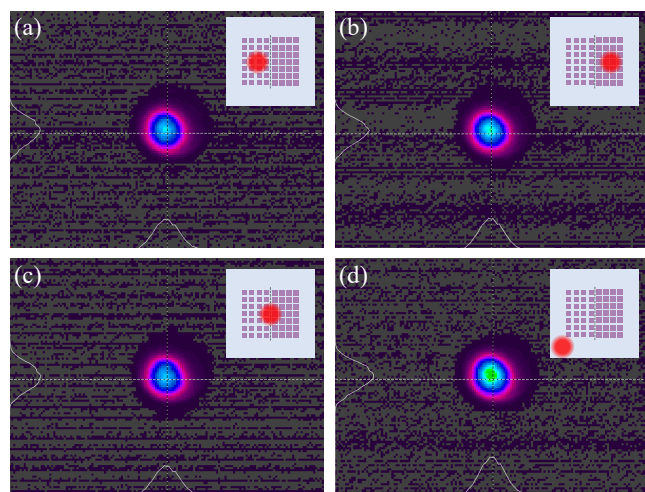


Figure S10: Pump beam spatial profile after interacting with (a) region A. (b) region B. (c) the center between the two regions. (d) the glass substrate. The pump beam retained its Gaussian profile in all cases confirming that spatial mode shaping occurs only for the SHG signal.